Materials Today • Volume xxx, Number xx • xxxx 2017

ELSEVIER

Printing continuous metal structures via polymer-assisted photochemical deposition

Zhi Zhao [1,2,3,*], Jing Bai [1], Yu Yao [1], Chao Wang [1,2,*]

[1] School of Electrical, Computer and Energy Engineering, Arizona State University, Tempe, AZ 85287, USA
[2] Center for Molecular Design and Biomimetics at the Biodesign Institute, Arizona State University, Tempe, AZ 85287, USA
[3] College of Materials Science and Engineering, Key Laboratory of Advanced Functional Materials, Education Ministry of China, Beijing University of Technology, Beijing, 100124, China

Patterning complex metallic structures via additive manufacturing (AM) has broad applications in energy, medical and aerospace industries. Current AM methods are often limited by high processing temperature, discontinuous film deposition and/or low product conductivity and reflectivity. We present a versatile room-temperature metal printing technique based on polymer-assisted photochemical deposition (PPD). Two-dimensional (2D) and three-dimensional (3D) printing of silver, gold and platinum structures with feature sizes as small as 5 μm are demonstrated on various substrates, including silicon, glass, polymers and biocompatible hydrogels. The PPD-printed metal films are continuous and smooth (roughness <3 nm) even at ultra-low thicknesses (<10 nm), and highly conductive ($\sim 3\times10^5$ S cm^{-1}) and reflective comparable to that of vacuum deposited counterparts. This breakthrough in advanced AM technique holds great promise for low-cost, fast and distributed manufacturing in optics, electronics and robotics.

Keywords: Two-dimensional; Metallic nanocrystals; Renewable energy; Electrocatalysis

Introduction

Programmable microfabrication of metallic structures is highly desired in integrated circuits [1], wearable electronics [2], plasmonics [3], bioscience [4] and sensing applications [5]. Conventional metal patterning demands specialized tools and complex processing steps [6,7], which are not suitable for low-cost production and prototyping. Additive manufacturing (AM) is advantageous in fast and economic production, since it allows a direct unit-by-unit deposition without requiring a mask or template [8,9]. The mainstream AM based metal printing techniques rely on thermal or laser-induced fusion of nozzle-deposited metal particles [10–12]. However, the high-temperature in fusion processes [12–14] is incompatible with most organic materials or water-rich soft materials (e.g. hydrogels), which possess great significance in flexible electronics, soft robotics and bio-sensors. In addition, there is still a challenge on tuning the viscoelastic properties of metal inks to minimize their droplet spreading, enable high-resolution printing and eliminate clogging of nozzles.

Optical 3D printing based on modulated light projection, including projection stereolithography (PSL) [15,16], computed axial lithography [17] and holographic 3D fabrication [18], has drawn tremendous attentions owing to its advantages. First, it features ultra-fast 3D printing due to the layer-by-layer or volumetric fabrication mechanism. Second, the nozzle-free setup allows for the fabrication of micrometer- to centimeter-scale structures by tuning the magnification of light projection [19]. Last but importantly, optical printing operates under ambient conditions and therefore is applicable to a broad range of materials, especially polymers and responsive materials [20,21]. Nevertheless, previous attempts on fabricating metallic patterns

* Corresponding authors.
E-mail addresses: Zhao, Z. (zzhao71@asu.edu; zhaozhi@bjut.edu.cn), Wang, C. (wangch@asu.edu).

 https://doi.org/10.1016/j.mattod.2020.03.001

Please cite this article in press as: Z. Zhao et al., Materials Today (2020), https://doi.org/10.1016/j.mattod.2020.03.001

List of abbreviations

Abbreviation	Full name
2D	two-dimensional
3D	three-dimensional
AAm	allylamine
AFM	atomic force microscopy
AgNP(s)	silver nanoparticle(s)
AM	advanced manufacturing
ASU	Arizona State University
CMOS	complementary metal oxide semiconductor
DLP	dynamic light projector
EBD	electron beam deposited
EDX	energy-dispersive X-ray
FWHM	full-width at half maximum
MNP(s)	metal nanoparticle(s)
PAAm	polyallylamine
PDMS	polydimethylsiloxane
PPD	polymer-assisted photochemical deposition
PS	polystyrene
PSL	projection stereolithography
RMS	root mean square
SEM	scanning electron microscopy
UV	ultraviolet
UV–Vis	ultraviolet–visible

by optical printing only produced aggregations of nanoparticles instead of continuous and smooth films [22,23]. Metallic structures formed by aggregated nanoparticles were highly porous with extensive defects, resulting in high optical loss [22,23] and poor electrical conductivity [12,13].

Here we present a novel annealing-free metal printing technique named polymer-assisted photochemical deposition (PPD). PPD prints continuous metal structures directly out of aqueous precursors under programmed ultraviolet (UV) illuminations at ambient conditions, which eliminates current challenges in AM based metal printing. Uniquely, a ligand-rich polymer is introduced to guide metal nanoparticle (MNP) assembly and growth. PPD is demonstrated in printing silver (Ag), gold (Au) and platinum (Pt) on various substrates. Metal patterns printed by PPD possess small surface roughness (down to 3 nm), high reflectivity (up to 95%), and high conductivity (3×10^5 S cm^{-1}), all comparable to vacuum-deposited counterparts. Notably, PPD is versatile in fabricating ultrathin films (<10 nm), complex microstructures down to 5 μm and 3D features on curved surfaces. The above merits make PPD ideal for developing prototypes functional composite materials.

Results and discussion

In our study, a PSL printer was employed for demonstration (Fig. 1a). Briefly, computer-designed structures were reconstructed by a series of 2D illuminations within a precursor solution using a UV (385 nm) dynamic light projector (DLP). The precursor was contained between a substrate and a transparent glass window. A typical metal precursor contains a metal salt, a small-molecule reductant, and a polymeric reactant to enable room temperature photochemical metal printing. In particular, metal ions are firstly reduced to MNPs via photo-reduction in the presence of the small-molecule reductant. The MNPs are then in-situ tethered by the polymer, proceed to enlargement via

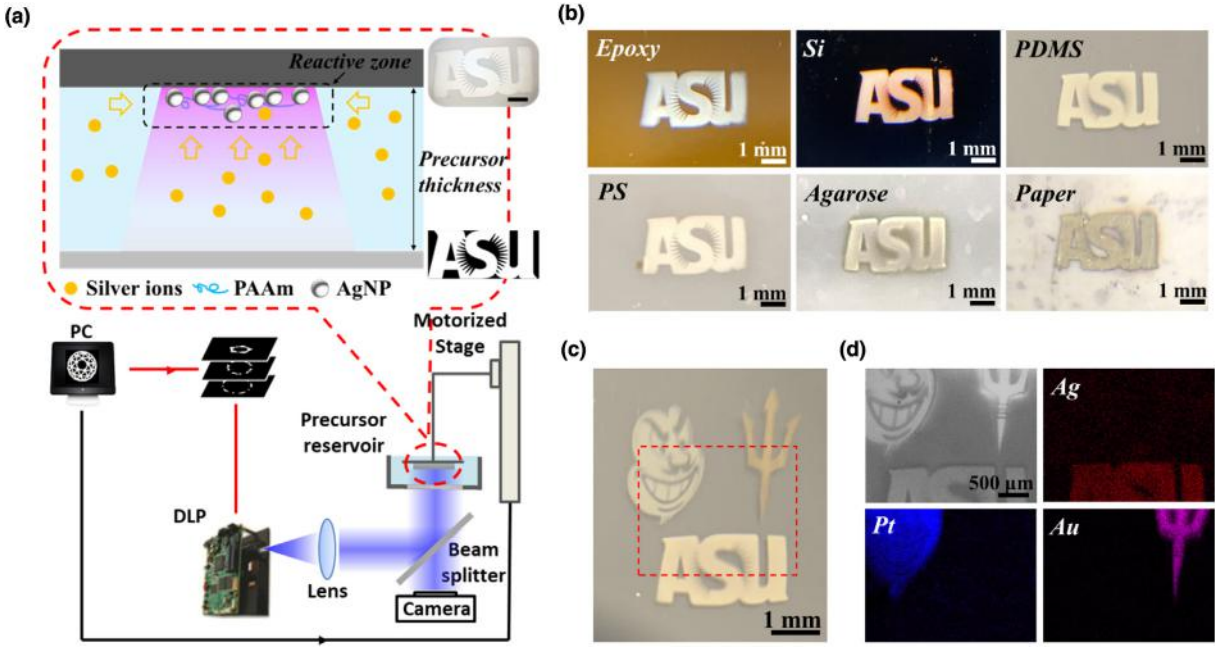

FIGURE 1

Polymer-assisted photochemical deposition (PPD). (a) Scheme of the printing setup and an example of printing an ASU logo. Scale bar: 500 μm. (b) Metal patterns printed on various substrates. (c) Printed ASU logo patterns containing multiple metallic materials. ASU mascot "Sparky": Pt. The pitchfork: Au. ASU sunburst logo: Ag. (d) SEM image and EDX elemental mappings of the boxed region in (c).

Please cite this article in press as: Z. Zhao et al., Materials Today (2020), https://doi.org/10.1016/j.mattod.2020.03.001

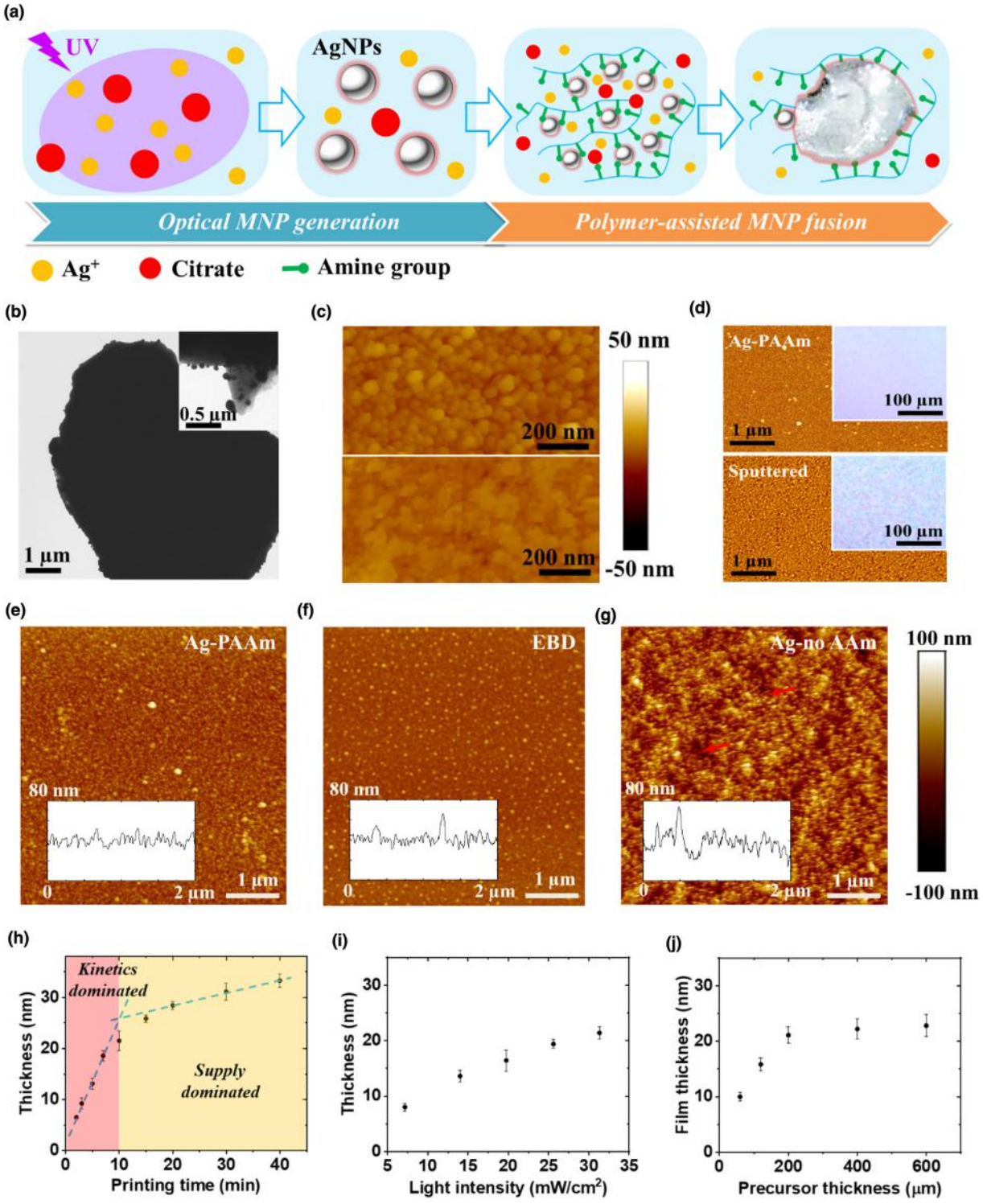

FIGURE 2

Investigations on the printing mechanism. (a) Hypothesized reaction mechanism of PPD. (b) TEM image of a micrometer-sized silver flake formed in the solution. Inset: magnified image of the edge of a flake. (c) AFM image of the top and bottom surface of printed Ag film. (d) Surface morphology of sub-10 nm silver films prepared by PPD and EBD. Top: AFM and microscopic image (inset) of a printed thin Ag film. Bottom: AFM and microscopic image (inset) of an EBD prepared thin Ag film. (e) Optically printed Ag film using Ag-PAAm precursor. Inset: AFM line scan. (f) EBD prepared Ag film. Inset: AFM line scan. (g) Optically printed Ag film using Ag-no PAAm precursor. Inset: AFM line scan. (h) Printed film thickness as a function of printing time. (i) Printed film thickness as a function of illumination intensity. (j) Printed film thickness as a function of precursor thickness.

Please cite this article in press as: Z. Zhao et al., Materials Today (2020), https://doi.org/10.1016/j.mattod.2020.03.001

seeded growth, and eventually form continuous materials as adjacent MNPs get connected via chemical reactions. The reactions only happen in an illumination defined reactive zone, therefore enables spatial patterning. The focusing and printing process were monitored by a CMOS camera in real time. The focal plane of UV illuminations was fixed at a constant level while the height of the substrate was adjusted using a motorized stage. By programming the projected light field, a silver Arizona State University (ASU) logo was printed onto a coverslip from a precursor containing silver nitrate, sodium citrate and polyallylamine (PAAm), which exhibited characteristic metallic color with faithfully reproduced fine features.

PPD is applicable to a wide variety of substrates (Fig. 1b), including glass, silicon, silicone, synthetic polymers (hydrophilic epoxy and hydrophobic polystyrene (PS)), papers and hydrogels. Silver ASU logos printed under the same conditions presented a very reflective outlook and high structural fidelity on most substrates except paper and agarose gel. The poorer printing quality on paper and agarose was attributed to their intrinsic surface roughness, which adversely affected light focusing (Fig. S1). Despite that, the successful printing of metallic features onto water-rich (e.g. 99 wt%) hydrogels was a very encouraging demonstration that remained elusive to date. Indeed, it is almost impossible to deposit metals onto hydrogels via conventional techniques due to substrates' significant structural deformation under vacuum or heat. The results hold promise for applications in biomolecular studies [24], food safety [25], and edible electronic devices [26].

Importantly, PPD can be generalized to print various metals by properly choosing the reactants. To prove the versatility of PPD, we printed Pt and Au micro-structures on glass. By introducing PAAm in a Pt precursor composed of ammonium tetrachloroplatinate(II) and ammonium iron(III) oxalate trihydrate, uniform Pt layers were successfully deposited onto glass substrates (Fig. S2a). In comparison, it was impossible to print Pt patterns without PAAm (Fig. S2b), as PAAm-free precursors could only yield Pt nanoparticles [27]. Similarly, gold patterns was produced using PAAm, gold(III) chloride trihydrate and sodium citrate (Fig. S2c), while only fragmented gold particles were deposited without PAAm (Fig. S2d). A common feature shared by Ag, Pt and Au is that their nanoparticles could all be synthesized using PAAm as a reducing and capping agent [28,29]. This indicated that a similar reaction pathway should be shared in printing those metals. It is possible to include different metallic elements in a product (Fig. S3) by simply switching metal precursors. As a proof-of-concept demonstration, we printed the ASU mascot "Sparky", the pitchfork, and the ASU sunburst logo in Pt, Au, and Ag, respectively (Fig. 1c). Scanning electron microscopy (SEM) image and energy-dispersive X-ray (EDX) mapping confirmed the elemental composition (Fig. 1d).

The reaction mechanism of PPD was studied using Ag as a model. Previous studies showed that both citrate and PAAm were able to reduce Ag^+ to AgNPs but not continuous film if used individually [30,31]. The UV-reduction of Ag^+ with citrate happened in seconds, which was highly desirable for fast metal printing [22,32]. However, the as-formed AgNPs were capped by negatively charged citrate ions, which prevented the interconnection of AgNPs due to columbic repulsions (Fig. S4a). On the other hand, PAAm capping layer was neutral and the aggregation of PAAm capped AgNPs could be tuned by adjusting Ag^+ to PAAm ratio [31,33]. This may be applied in continuous metal printing, if photo-responsiveness could be incorporated to PAAm based synthetic systems. Therefore, the synergic effect of citrate and PAAm should be the key to continuous metal growth.

We believe that silver printing by PPD involved a two-step reaction pathway, namely optical MNP generation and polymer-assisted MNP fusion (Fig. 2a). In the first step, small AgNPs formed in the presence of citrate ions and UV illumination, serving as seeds for future growth. Next, the MNPs bind to PAAm and grow into continuous crystalline structure. PAAm played two important roles. First, the long PAAm chain acted as a template to tether AgNPs into a cluster through the coordination between amine groups and silver [34]. Partial replacement of the initial citrate capping layer by PAAm decreases the surface charge density on AgNPs, and accordingly helps shorten the inter-particle distance, fix their relative positions, and promote interconnections between AgNPs. In comparison, only small AgNP aggregates were observed when allylamine (AAm) was employed (Fig. S4b). Apparently, AgNPs bound to AAm were still subject to Brownian motion in the solution and had diminished chance to be connected. Meanwhile, PAAm established an anisotropic chemical environment around AgNPs and served as a directional reducing agent [31,35]. Inter-particle crystal growth was favored due to higher accessibility of "seeds" and amine groups in the gap (Fig. 2a). As a result, large MNPs tended to form under the presence of PAAm. In a bulk solution investigation, UV–Vis spectra revealed that as the PAAm concentration in a silver precursor increased from 0 to 20 mM, the measured absorption broadened and red shifted, indicating the increase in particle size (Fig. S4c) [30,32]. This is further evidenced by TEM imaging that showed successful growth of micrometer-sized metal crystal under 20 mM PAAm (Fig. 2b). EDX analysis clearly indicated that the flake was Ag(0) from measured elementary composition (Fig. S4d). The presence of many AgNP clusters in the solution led to a three-dimensional interlaid network, which grew into macroscopic continuous Ag structures under continuous UV illumination and sufficient supplies of reagents. For example, silver film covering a reaction container could form under the above conditions (Fig. S4e).

In PSL setup, more physical and chemical processes could be involved due to the presence of a substrate and focused light, including anisotropic molecular diffusion, surface attachment of metal clusters, light scattering at interfaces, etc. (Fig. 1a) [36]. Although complete elucidation of all their effects is beyond the scope of this work, a simplified model could be used for qualitative understandings. Conceptually, printed metal grew in a layer-by-layer fashion (Fig. S5a). Metal growth initiates from the substrate surface due to the highest local light intensity and the energetically favorable attachment of PAAm-capped AgNPs (e.g. via hydrogen bond and Van der Waals interactions). Then the first AgNP layer facilitates the deposition of consequent layers. Consequently, the $(n-1)^{th}$ AgNP layer tends to form before the n^{th} layer gets deposited. Therefore, printed metal patterns would have a smaller surface roughness at the substrate due to longer reaction time and more sufficient chemical fusion but a more granulated look on the precursor side. To confirm this, the

Please cite this article in press as: Z. Zhao et al., Materials Today (2020), https://doi.org/10.1016/j.mattod.2020.03.001

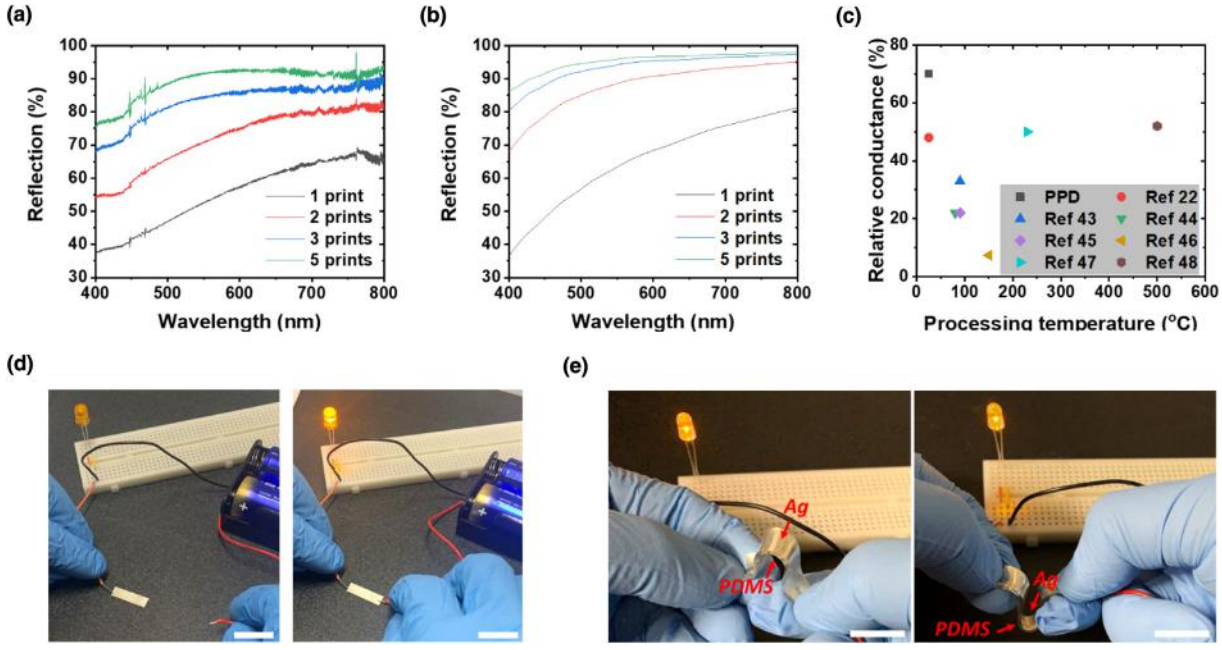

FIGURE 3

Characterization of optical and electrical performance of printed silver films. (a) Experimental reflectance of printed silver patterns. Each print added ~23.8 nm to the total metal thickness. (b) Simulated reflectance of various silver films. (c) Comparison of experimental conductivity of silver patterns fabricated by various metal printing methods. Conductivity was normalized with pure silver conductivity after considering the effect of boundaries. (d) Printed silver strip that lightened an LED bulb. Scale bars: 2 cm. (e) Conductivity of a bending strip. Scale bars: 2 cm.

top and bottom of printed silver films were examined by AFM following the protocol in Fig. S5b. The top surface of printed 23 nm-thick Ag films displayed a morphology of closely packed nanoparticles with a root mean square (RMS) of 5.6 nm, while the bottom surface showed up smoother morphology (RMS = 2.8 ± 0.5 nm) (Fig. 2c).

Due to the unique printing mechanism, PPD could outperform conventional evaporative and sputtering deposition techniques in fabricating very thin metal films. Silver films prepared by PPD (6.6 nm on glass substrates) showed a much smoother surface (RMS = 3.3 nm) and better continuity than electron beam deposited (EBD) film (7.5 nm, RMS = 5.7 nm) under similar deposition rate (~2.3 nm min^{-1}), as examined by AFM (Fig. 2d). Gaseous phase deposited noble metal films contained isolated big islands as a result of interface energy minimization [37,38]. which displayed granulated morphology, non-uniform reflection, and plasmonic absorption (~480 nm) from AgNPs (Figs. 2d and S6). In comparison, various capping agents in PPD could stabilize small MNPs [39]. Consequently, the product behaved more like films (Fig. 2d and S6). We further compared thicker (>20 nm) silver films. The surface RMS of printed Ag film was 5.6 nm (Fig. 2e), comparable to that (5.2 nm) of EBD fabricated ones (Fig. 2f). The vacuum-deposited thick film was relatively smooth compared with thin films because of atom migration and crystal growth [38]. Silver film printed without PAAm exhibited a much rougher surface with many voids (Fig. 2g), coincident with previous findings [22,23]. The 3D profile of metal films fabricated by different methods is shown in Fig. S7, which indicates the high continuity and quality of Ag films printed by PPD.

We investigated the impact of several experimental parameters, including illumination time, light intensity and precursor thickness, on metal printing rate. As the chemicals within the reactive zone are consumed, a chemical gradient is established. Reagents in the surrounding solution will diffuse into the reactive zone, which in turn supports continuous Ag growth (Fig. 1a). AFM measurements showed that there are two regimes of different growth rate versus printing time (Fig. 2h). The initial fast deposition (~2.3 nm min^{-1}) within 10 min corresponded to a reaction-kinetics dominated stage during which the reagents' concentration was sufficiently high. At this time, the printing rate was mainly determined by the number of available photons that triggered the reaction. As the reagents were consumed with time, the reagents' concentration became the rate limiting factor, leading to a constant printing rate roughly identical to the diffusion rate after ~20 min (Fig. S8).

Light intensity determined the photo-reduction rate and affected the overall growth rate (Fig. 2i), which has been observed in the synthesis of many metallic nanomaterials [30,40]. Here we fixed the printing time at 10 min, which fell into the kinetics-dominated zone. As can be seen, the film thickness almost increased linearly with the illumination intensity, confirming that the printing rate was limited by available photons. It is also found that below ~7 mW cm^{-2} (an "intensity threshold"), no silver film was formed. This could be attributed to the reason that when the photo-reduction was too slow, the AgNP density was insufficient to support film formation. This intensity threshold defined the boundary of reactive zone. Increasing the thickness of precursor had minimal effect on the reaction rate when the thickness of precursor was greater than

Please cite this article in press as: Z. Zhao et al., Materials Today (2020), https://doi.org/10.1016/j.mattod.2020.03.001

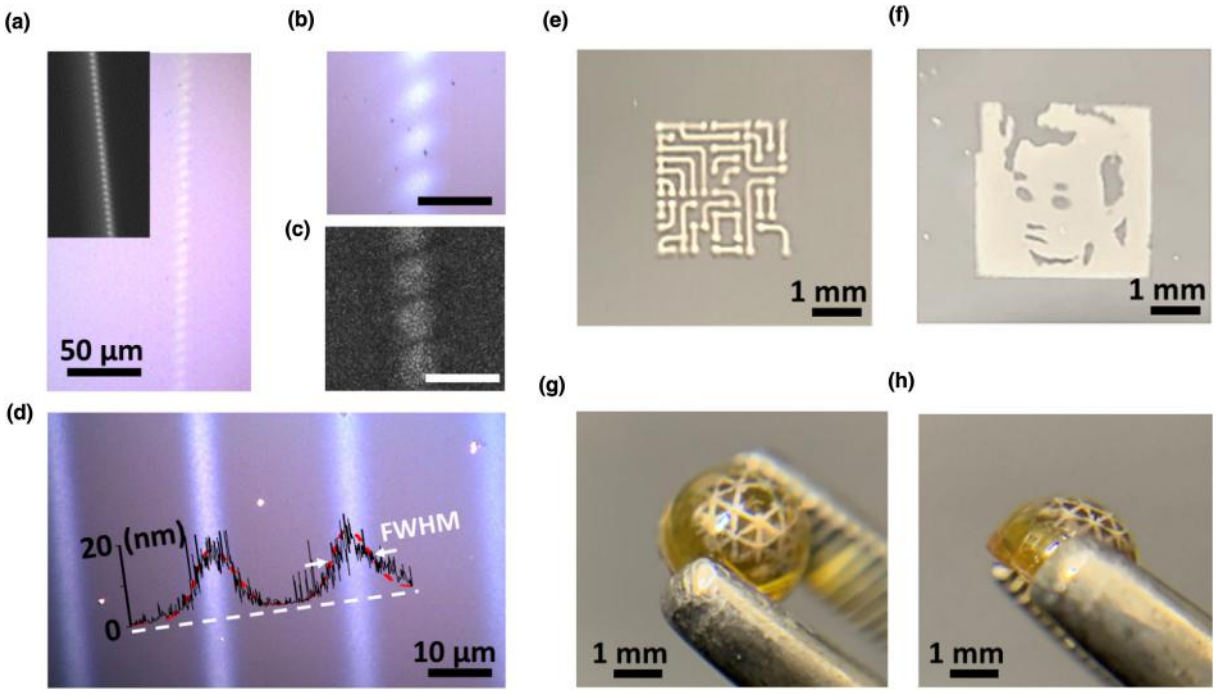

FIGURE 4

Printing of microstructures and 3D patterns. (a) Microscopic images of a printed single pixel line. Inset: The corresponding optical pattern. (b) A magnified image of (a). Scale bar: 10 μm. (c) SEM image of the sample in (a). Scale bar: 10 μm. (d) Optical image overlaid with AFM height profile of a printed grating. White dashed line indicates the position of AFM line scan. (e) Printed electronic circuits. (f) Portrait of a toddler. (g and h) Silver network on top of a hemisphere.

that of reactive zone (Fig. 2j). For example, as the precursor thickness tripled from 200 μm to 600 μm, the film thickness only increased by ~10%. On the other hand, the metal thickness was highly dependent on the precursor thickness when it was below 200 μm, indicating a ~200 μm-thick reactive zone.

The above results also indicated that printing thick film could be too time-consuming if operating in the diffusion limited regime (Fig. 2h). In practice, one may replenish the solution and conduct multiple short printings. Our preliminary data revealed that the accumulative thickness showed a decent linear relationship with the number of printing cycles (Fig. S9), making our technique suitable for both thin and thick metallic patterns.

Silver patterns fabricated by PPD demonstrated an extraordinary quality, making them suitable for optical and electronic applications (Fig. 3). The reflection of a series of printed silver films were examined under a UV–Vis spectrometer. The average reflectance reached >50% above 500 nm for one print, which increased to >90% for patterns made by five prints. FDTD simulations confirmed that the experimental reflectance was very close to theoretical values, demonstrating the superior quality of printed Ag patterns (Fig. 3b). In fact, the measured reflectance in the visible spectrum after 5 printing cycles was comparable to that of commercial silver mirrors (Fig. S10a). Ag films prepared by PPD had great uniformity and repeatability, as confirmed by spectral and AFM measurements (Fig. S10b and c).

We also measured the conductivity of printed silver patterns using four-probe method (Fig. S11). The measured conductivity was 3.1×10^7 S m^{-1} (Figs. 3c and S12), which was 72% of vacuum-deposited silver film of equal thickness (~4.3×10^7 S m^{-1}) [41]. This is close to the theoretical conductivity of Ag film (4.5×10^7 S m^{-1}, Supplementary Section 7) considering the reduced electron mean free path at boundaries [42,43]. In comparison, none of the previously demonstrated printing technique was able to achieve the same conductivity (Fig. 3c) [22,44–49]. With this superior electrical property, electronic devices could be easily constructed by PPD. In a proof of concept demonstration, we replaced a portion of an electronic circuit by a printed silver strip on polydimethylsiloxane (PDMS). An LED light bulb was lit up by printed wires, demonstrating their electrical conductivity (Figs. 3d and S13). Interestingly, the silver strips maintained good conductivity even bent 180° concavely or convexly (Fig. 3e). This behavior was different from previous findings [22] where bending could cause significant conductivity loss to AgNPs films (Fig. S14). Such a deformation tolerance in the conductivity was ideal for flexible electronics. A comparison of the performance of various metal printing techniques was shown in Table S1, which demonstrated the advantages of PPD over the other methods.

We further studied the printing resolution in PPD (Fig. S15). A detailed discussion is provided in Supplementary Section 9. As shown in Fig. 2h, the metal deposition could happen within a relatively short time (e.g. a few minutes) during which the diffusion of MNPs was minimal [50]. In addition, the presence of PAAm facilitated AgNP clustering, which further minimized particle diffusion. In this case, it is possible to printed patterns down to a few μm. Straight lines of a single pixel wide were printed on glass substrates and clearly visualized (Fig. 4a and b). SEM image (Fig. 4c) indicated that each printed metal pixel was about

Please cite this article in press as: Z. Zhao et al., Materials Today (2020), https://doi.org/10.1016/j.mattod.2020.03.001

~5 μm × 5 μm and well resolved when using a 10× objective lens with numerical aperture (NA) of 0.3. By using a 20x objective lens with NA = 0.5, the pixel size was reduced to ~2.5 μm × 2.5 μm and metal gratings with a period of 24 μm could be printed (Fig. 4d). Using a designed line width of two pixels, the measured linewidth at its full-width at half maximum (FWHM) was 8 μm or ~3.2 pixels, indicating the overall broadening was about 1.5 μm in each direction. The above results demonstrated the resolution of PPD was at least 3 μm (2 × 1.5 μm) under the current experimental conditions, and might be further improved by reducing the imaging pixel size and eliminating particle diffusion.

Complex patterns, such as electronic wires and portraits could be readily printed by PPD (Fig. 4e and f). Particularly, by pixelating and digitizing colored images (Fig. S15), it is possible to print digital designs from demand (Fig. 4f). Furthermore, by programming the focal plane and conducted a layer-by-layer deposition (Fig. S16), we were also able to construct 3D metallic features on curved surfaces of an epoxy hemisphere (Fig. 4g and h). In comparison, conventional photolithography and metal vacuum deposition methods are not ideal for high-resolution 3D patterning because of the fixed focus in photolithography and the directional material flux in vacuum system.

Conclusions

In summary, we demonstrated a general strategy to optically print metallic features under ambient conditions by PPD. The effect of critical experimental parameters, including illumination intensity, exposure time and precursor thickness has been investigated. The two-step reaction converted MNPs to smooth and continuous materials, whose electrical and optical properties were similar to vacuum deposited metals. PPD was applicable to printing a number of noble metals (with silver, gold, and platinum demonstrated in this work) on a variety of substrate materials (including glass, silicon, polymer, and hydrogels), producing ultrathin and smooth films and micrometer scale high-resolution images, and generating complex and 3D patterns. With the low cost, high printing quality and excellent versatility, we expect PPD to find applications in, but not limit to, soft robotics, biochemical sensors, responsive coatings, solar harvesting devices, intelligent electromagnetic devices, smart biomedical devices, and energy storage devices.

Materials and methods

Metallic patterns were printed in a layer-by-layer fashion following a previously-established protocol [19]. In general, a substrate was dipped into a reservoir filled with silver precursors. A desired light pattern was illuminated from the bottom through a transparent window to cure the precursor layer between the substrate and the window (Fig. 1a). The window was a cover glass modified with a layer of (tridecafluoro-1,1,2,2-tetrahydrooctyl)triethoxysilane as non-sticky coating. A DLP® LightCrafter™ E4500 MKII™ development module with 385 nm emission was employed as the light source, whose maximum output power was 2 W. In order to achieve the optimal printing efficiency, each printing cycle lasted for 10 min with the light intensity set to be 31.3 mW cm^{-2}. After the first layer was cured, the height of the substrate was adjusted using a motorized stage so the second layer (if applicable) could be cured in the same manner. After the completion of printing, the product was removed from the reservoir, rinsed with DI water and dried in N_2 flow. The thickness and surface morphology of optically printed silver patterns were examined by a Bruker Multimode 8 AFM. Optical images, as well as reflection and transmission spectra of the same films were recorded with an Olympus BX53 fluorescent microscope coupled Horiba iHR320 imaging spectrometer. The relative reflection of samples was calculated using raw spectral data and a protected silver mirror (Thorlabs) as reference.

More details about materials and methods can be found in the supporting information.

CRediT authorship contribution statement

Zhi Zhao: Conceptualization, Methodology, Investigation, Validation, Formal analysis, Supervision, Writing - original draft, Writing - review & editing. **Jing Bai:** Investigation, Validation, Formal analysis, Writing - review & editing. **Yu Yao:** Formal analysis, Supervision, Writing - review & editing. **Chao Wang:** Formal analysis, Supervision, Writing - original draft, Writing - review & editing, Funding acquisition.

Acknowledgements

We thank Prof. Hao Yan and Prof. Yan Liu for sharing their AFM and lab space. C.W. thanks the ASU startup funds and National Science Foundation [grant number 1711412] for supporting this research.

Appendix A. Supplementary data

Details of materials and experimental methods; schemes of the reaction mechanism; and details of the data analysis. Supplementary data to this article can be found online at https://doi.org/10.1016/j.mattod.2020.03.001.

References

[1] B.C.K. Tee et al., Science 350 (2015) 313–316, https://doi.org/10.1126/science.aaa9306.
[2] S. Wang et al., Nature 555 (2018) 83–88, https://doi.org/10.1038/nature25494.
[3] Z. Zhao et al., ACSNano 11 (2017) 6594–6604, https://doi.org/10.1021/acsnano.6b07867.
[4] C.Y. Chen et al., Nanoscale 10 (2018) 3191–3197, https://doi.org/10.1039/C7NR07381J.
[5] A.M. Andrews, W.S. Liao, P.S. Weiss, Acc. Chem. Res. 49 (2016) 1449–1457, https://doi.org/10.1021/acs.accounts.6b00034.
[6] A. Nemiroski et al., ACSNano 8 (2014) 11061–11070, https://doi.org/10.1021/nn504214b.
[7] P. Nagpal et al., Science 325 (2009) 594–597, https://doi.org/10.1126/science.1174655.
[8] I. Gibson, D.W. Rosen, B. Stucker, Additive Manufacturing Technologies, Springer, New York, 2010.
[9] B.P. Conner et al., Addit. Manuf. 1 (2014) 64–76, https://doi.org/10.1016/j.addma.2014.08.005.
[10] A.D. Valentine et al., Adv. Mater. 29 (2017) 1703817, https://doi.org/10.1002/adma.201703817.
[11] J.H. Martin et al., Nature 549 (2017) 365–369, https://doi.org/10.1038/nature23894.
[12] Y. Son et al., Adv. Mater. 23 (2011) 3176–3181, https://doi.org/10.1002/adma.201100717.2009.
[13] B.Y. Ahn et al., Science 323 (2009) 1590–1593, https://doi.org/10.1126/science.1168375.
[14] M.A. Skylar-Scott, S. Gunasekaran, J.A. Lewis, PNAS 113 (2016) 6137–6142, https://doi.org/10.1073/pnas.1525131113.

Please cite this article in press as: Z. Zhao et al., Materials Today (2020), https://doi.org/10.1016/j.mattod.2020.03.001

[15] P.F. Jacobs, Rapid Prototyping & Manufacturing: Fundamentals of Stereolithography, Society of Manufacturing Engineers, Dearborn, 1992.
[16] D. Han et al., Addit. Manuf. 27 (2019) 606–615, https://doi.org/10.1016/j.addma.2019.03.031.
[17] B.E. Kelly et al., Science 363 (2019) 1075–1079, https://doi.org/10.1126/science.aau7114.
[18] M. Shusteff et al., Sci. Adv. 3 (2017) eaao5496, https://doi.org/10.1126/sciadv.aao5496.
[19] J.R. Tumbleston et al., Science 47 (2015) 1349–1352, https://doi.org/10.1126/science.aaa2397.
[20] V.A. Liu, S.N. Bhatia, Biomed. Microdevices 4 (2002) 257–266, https://doi.org/10.1023/A:1020932105236.
[21] Y. Lu et al., J. Biomed. Mater. Res. Part A 77 (2006) 396–405, https://doi.org/10.1002/jbm.a.30601.
[22] X. Yang et al., Adv. Funct. Mater. 29 (2019) 1807615, https://doi.org/10.1002/adfm.201807615.
[23] Y. Zhang et al., ACSNano 12 (2018) 9913–9921, https://doi.org/10.1021/acsnano.8b02868.
[24] P. Zucca, R. Fernandez-Lafuente, E. Sanjust, Molecules 21 (2016) 1577, https://doi.org/10.3390/molecules21111577.
[25] L.M. Barrangou, C.R. Daubert, E.A. Foegeding, Food Hydrocolloids 20 (2006) 184–195, https://doi.org/10.1016/j.foodhyd.2005.02.019.
[26] W. Xu et al., Adv. Mater. Technol. 2 (2017) 1700181, https://doi.org/10.1002/admt.201700181.
[27] L.D. Zarzar et al., J. Am. Chem. Soc. 134 (2012) 4007–4010, https://doi.org/10.1021/ja211602t.
[28] G. Fu et al., Phys. Chem. Chem. Phys. 15 (2013) 3793–3802, https://doi.org/10.1039/c3cp44191a.
[29] J.D.S. Newman, G.J. Blanchard, J. Nanopart. Res. 9 (2007) 861–868, https://doi.org/10.1021/la060045z.
[30] R. Jin et al., Science 294 (2001) 1901–1903, https://doi.org/10.1126/science.1066541.
[31] P.L. Kuo, W.F. Chen, J. Phys. Chem. B 107 (2003) 11267–11272, https://doi.org/10.1021/jp030116s.
[32] R. Sato-Berrú et al., J. Raman Spectrosc. 40 (2009) 376–380, https://doi.org/10.1002/jrs.2135.
[33] Z. Wu, S. Yang, W. Wu, Nanoscale 8 (2016) 1237–1259, https://doi.org/10.1039/C5NR07681A.
[34] Z. Zhao et al., J. Mater. Chem. C 7 (2019) 6099–6104, https://doi.org/10.1039/C9TC01473J.
[35] R. Sardar, J.W. Park, J.S. Shumaker-Parry, Langmuir 23 (2007) 11883–11889, https://doi.org/10.1021/la702359g.
[36] N.T.K. Thanh, N. Maclean, S. Mahiddine, Chem. Rev. 114 (2014) 7610–7630, https://doi.org/10.1021/cr400544s.
[37] C.V. Thompson, R. Carel, J. Mech. Phys. Solids 44 (1996) 657–673, https://doi.org/10.1016/0022-5096(96)00022-1.
[38] I. Petrov et al., J. Vac. Sci. Technol. A 21 (2003) S117–S128, https://doi.org/10.1116/1.1601610.
[39] E. Jiran, C.V. Thompson, J. Electron. Mater. 19 (1990) 1153–1160, https://doi.org/10.1007/BF02673327.
[40] B.C. Huang et al., Sci. Rep. 9 (2019) 1–11, https://doi.org/10.1371/journal.pone.0167937.
[41] J.W.C. De Vries, Thin Solid Films 167 (1988) 25–32, https://doi.org/10.1016/0040-6090(88)90478-6.
[42] K. Fuchs, Math. Proc. Cambridge Philos. Soc. 34 (1938) 100–108, https://doi.org/10.1017/S0305004100019952.
[43] D.S. Campbell, A.R. Morley, Rep. Prog. Phys. 34 (1971) 283–368, https://doi.org/10.1088/0034-4885/34/1/305.
[44] H. Xu et al., Conductivity of silver and copper film printed by particle-free reactive inks, in: 2017 18th International Conference on Electronic Packaging Technology (ICEPT), 2017, pp. 1470–1473.
[45] T. Yamada et al., Nat. Commun. 7 (2016) 11402, https://doi.org/10.1038/ncomms11402.
[46] A. Mamidanna et al., ACS Appl. Mater. Interfaces 8 (2016) 12594–12598, https://doi.org/10.1021/acsami.6b03922.
[47] J. Liang, K. Tong, Q. Pei, Adv. Mater. 28 (2016) 5986–5996, https://doi.org/10.1002/adma.201600772.
[48] A.J. Kell et al., ACS Appl. Mater. 9 (2017) 17226–17237, https://doi.org/10.1021/acsami.7b02573.
[49] D. Jang et al., Adv. Funct. Mater. 18 (2008) 2862–2868, https://doi.org/10.1002/adfm.200800238.
[50] S. Albaladejo, M.I. Marqués, J.J. Sáenz, Opt. Express 19 (2011) 11471–11478, https://doi.org/10.1364/OE.19.011471.

Please cite this article in press as: Z. Zhao et al., Materials Today (2020), https://doi.org/10.1016/j.mattod.2020.03.001